

Low-SWaP Magneto-optical Trap using both Planar Optical and Magnetic Components

Hao Gao^{1,†}, Yumeng Zhu^{2,†}, Zhilong Yu², Yuhui Hu¹, Zhelin Lin¹, Shiming Wei², Feng Zhao²,
Amit Agrawal^{3,4}, Zeyang Liu^{1*}, Xiaochi Liu^{2*}, and Cheng Zhang^{1*}

¹School of Optical and Electronic Information & Wuhan National Laboratory for Optoelectronics, Huazhong University of Science and Technology, Wuhan 430074, China

²Key Laboratory of Atomic Frequency Standards, Innovation Academy for Precision Measurement Science and Technology, Chinese Academy of Sciences, Wuhan 430071, China

³Department of Engineering, University of Cambridge, Cambridge CB3 0FA, U.K.

⁴Kyung Hee University, 26 Kyunghedae-ro, Dongdaemun-gu, Seoul 02447, Korea

[†]Equal contributors

*Email: zeyangliu@hust.edu.cn; liuxc@apm.ac.cn; cheng.zhang@hust.edu.cn

Abstract

Compact, lightweight, and energy-efficient cold atom systems are crucial for advancing quantum technologies, yet their realization remains constrained by the bulky optical and magnetic components required in current atom trapping architectures. Here, we demonstrate a low-SWaP (size, weight, and power) magneto-optical trap that seamlessly integrates planar optical and magnetic components into a unified platform. A monolithic dual-functional metasurface simultaneously polarizes and shapes the cooling beam, replacing traditional lens–waveplate assemblies and converting a linearly polarized Gaussian beam into a circularly polarized flat-top beam. In parallel, a planar coil chip substitutes bulky anti-Helmholtz coils and generates the required quadrupole magnetic field with drastically reduced power consumption. Under D₂-line cooling of ⁸⁷Rb atoms, the fully planar system delivers nearly an order-of-magnitude improvement in trapping performance while operating at a fraction of the size, weight, and power of traditional systems. This compact, bulky-component-free approach offers a scalable, energy-efficient pathway toward chip-scale cold-atom platforms.

Keywords: cold atom, magneto-optical trap, metasurface, laser cooling, magnetic coil chip

Introduction

Cold atoms (*1-3*), i.e., atoms which are cooled to near absolute zero temperatures and exhibit significantly reduced atomic motion, enable the observation of various quantum phenomena and are crucial in an array of applications including precise timekeeping (*4, 5*), quantum computing (*6*), and quantum sensing (*7*). Current atom cooling and trapping methods include Optical Molasses (*8*), Dipole Traps (*9*), Optical Lattices (*10*), and Magneto-Optical Traps (MOTs) (*11*). Among them, MOTs combine magnetic field and laser beams to efficiently create a large population of cooled and trapped atoms, and therefore, stand out as a robust and widely used technique nowadays. In a typical three-dimensional (3D) MOT system, the trap is established within a vacuum environment via scattering forces created by several laser cooling beams and a closed magnetic trap generated by a pair of anti-Helmholtz coils (*12, 13*). Such configuration typically involves three pairs of counter-propagating laser beams having orthogonal circular polarization states, alongside a quadrupole magnetic field. To construct such MOT system, a series of optical components, like mirrors, prisms, beam splitters, and waveplates, are required to deliver the laser cooling beams along their designed paths and prepare appropriate polarization states for them. At the same time, anti-Helmholtz coils are commonly employed to generate the quadrupole magnetic field, which inevitably occupy considerable space and weight. Such bulky and intricate configuration presents challenges for integrating MOTs into low-SWaP (size, weight, and power) systems that rely on cold atoms as core components. Consequently, recent efforts have aimed at the miniaturization of various MOT components, leading to the development of pyramid-shaped MOTs (*14, 15*), grating MOTs (GMOTs) (*16, 17*), Fresnel MOTs (*18*) and photonic integrated circuit (PIC)-based MOTs (*19, 20*). These approaches allow for the manipulation and delivery of laser beams

through miniature or on-chip components, effectively reducing the spatial footprint of laser cooling setups. Among them, the GMOT approach stands out for its robustness and simplicity, where a planar diffraction grating splits a single free-space laser beam into several intersecting beams and thus eliminates the need for multiple discrete laser sources. This technique has demonstrated feasibility across various compact and miniature cold atom-based quantum instruments, such as atomic clocks (21, 22), atomic interferometers (23), and quantum vacuum standards (24).

Although the GMOT approach simplifies laser cooling by eliminating the need for multiple discrete laser beams, it imposes more stringent requirements on the laser cooling beams compared to conventional MOT techniques. Taking a 4-comb-shaped GMOT system (25) as an example, the schematic of a cooling setup with conventional optical and magnetic components is illustrated in the left panel of Fig. 1A. The laser beam is conditioned into the required cooling geometry and directed onto the grating chip through a series of bulky optical components. The incident laser beam and the corresponding diffracted beams by the grating chip intersect inside the vacuum cell, achieving equilibrium at the center of the quadrupole magnetic field created by a pair of anti-Helmholtz coils. Due to the periodic structure of the grating chip and the need to balance scattering forces by the incident and diffracted laser beams, the incident laser beam needs to have a circular polarization state and a close-to-uniform intensity distribution for the GMOT to function properly (26-29). However, typical output beams from laser sources or fiber collimators are linearly polarized and exhibit Gaussian intensity profiles, which would disrupt the scattering force balance in the beam intersection region and thus degrade the laser cooling efficiency. To mitigate this issue, additional optical components are necessary to adjust the beam's polarization state and intensity profile. A quarter-

wave plate (QWP) is typically employed to convert the beam's polarization state into circular. At the same time, a lens (or a series of lenses) can be used to expand the Gaussian beam so that only its central region—having a more uniform intensity profile—illuminates the grating chip (25, 30). While effective, this method inevitably consumes considerable space and results in significant waste of light energy. Additionally, it is prone to cause imbalance in the scattering forces among the intersecting beams generated by the grating chip (26). In parallel, most GMOT systems still rely on conventional anti-Helmholtz coils for the quadrupole magnetic field generation, which also demands substantial space and precise adjustment. Despite recent efforts to reduce the volume and power consumption of conventional anti-Helmholtz coils (31-34), most approaches still rely on discrete or three-dimensional structures, resulting in a structural mismatch with miniature cold atom systems. Obviously, these space-consuming optical and magnetic components contradict the GMOT's intended goal of system miniaturization. Addressing this challenge requires the development of alternative optical and magnetic elements that can deliver equivalent or even improved performance with higher energy efficiency, reduced footprint, and lower weight.

Here, we present a high-performance, low-SWaP GMOT architecture that eliminates the need for bulky, three-dimensional components with isolated functionalities by seamlessly integrating planar, multi-functional optical and magnetic elements into a unified platform (Fig. 1A, right panel). Our miniaturization strategy relies on two key innovations: (i) a dielectric metasurface that simultaneously performs beam shaping and polarization control, thereby replacing separate lenses and waveplates; and (ii) a lithographically fabricated planar coil chip that generates the required quadrupole magnetic field, effectively substituting bulky anti-Helmholtz coil pairs. Specifically, we implement a transmission-type silicon (Si) metasurface

that transforms a linearly polarized Gaussian beam ($\lambda = 780$ nm) into a circularly polarized flat-top beam (FTB) whose cross-sectional area is precisely matched to the grating chip. The resulting FTB exhibits 78.58% intensity uniformity, a root-mean-square intensity variation of 8%, and a circular polarization degree of 98.64%. In parallel, we develop a 2-mm-thick coil chip consisting of 10 stacked layers of coplanar annular coils. The coil chip is fully planar, structurally compatible with the grating chip, and generates a magnetic field gradient of 11.7 Gs/cm at only 0.56 W of power consumption—whereas conventional anti-Helmholtz coils typically require several tens of watts to achieve similar gradients. Compared to conventional GMOT systems using expanded Gaussian beams, the proposed system reduces the volume and weight of the core optical and magnetic components by several orders of magnitude. At the same time, it achieves $1.8 - 3.5\times$ higher trapped atom counts at equal laser power and captures up to $(8.15 \pm 0.15) \times 10^6$ ^{87}Rb atoms at 100 mW, demonstrating significantly improved trapping efficiency. This fully planar integration strategy provides a practical pathway to low-SWaP cold-atom platforms, with strong potential for miniature or chip-scale atomic clocks, field-deployable interferometers, and spacecraft-based quantum instruments.

Results

Moving from conventional GMOT systems to low-SWaP GMOT systems

The proposed low-SWaP GMOT system integrates two key planar elements: a dielectric metasurface (Fig. 1B, top panel) and a planar coil chip (Fig. 1B, bottom panel). Before we elaborate on the details of these two planar elements, we will analyze and compare the scattering forces exerting on the ^{87}Rb atoms (which are the atoms being cooled and trapped in this study) by a Gaussian beam (employed in a conventional GMOT system) and a flat-top beam (employed in the proposed low-SWaP GMOT system), respectively.

The grating chip for single laser cooling typically consists of three linear gratings symmetrically arranged at 120° angles to form a triangular configuration (Fig. 1B, middle panel). The grating is periodically etched, where each etched groove has identical structural parameters. The scattering forces exerted by the single incident beam and three diffracted beams can be denoted as F_i and F_{d_j} (where $j = 1, 2, 3$), respectively (Fig. 1B, middle panel). The angles between $F_{d_{1,2,3}}$ and the z -axis equal to the grating diffraction angle θ . The components of F_{d_1} , F_{d_2} , and F_{d_3} in the horizontal plane (the xy plane) are separated by an angle of 120° with respect to each other. In this comparative study, the spatial intensity distribution of the beam illuminating over the square area of the grating chip (with a side length of 20 mm) is set to be either a flat-top profile (with a side length of $L = 20$ mm, identical to that of the grating chip) or a Gaussian profile (with a cross-sectional diameter of $d = 20$ mm). Here, the beam diameter d is defined as twice the distance from the axis of the Gaussian beam to where its intensity drops to $1/e^2$ ($\approx 13.5\%$) of the maximum value. In the subsequent comparison, the total energy of the incident beam irradiated on the grating chip area is set to be the same,

regardless of the beam profile or size.

Figure 1C shows the spatial intensity distribution on the yz plane (perpendicular to the grating chip), resulting from the interaction of incident and diffracted laser beams. When the incident beam has a flat-top profile, the GMOT region exhibits a uniform spatial intensity distribution across the yz plane (Fig. 1C, left panel). In contrast, when the incident beam has a Gaussian profile, the GMOT region exhibits a characteristic intensity decay across the yz -plane, with beam intensity diminishing as a function of both radial distance from the grating chip center along the y -axis and vertical height above the grating chip surface along the z -axis (Fig. 1C, right panel).

We then examine the scattering force distributions under the two illumination configurations. On the xy -plane, the forces along the positive and negative halves of the x - and y -axes remain equal in magnitude and opposite in direction about the origin, independent of the illuminating beam's profile and size. In contrast, the scattering force distribution in the GMOT region displays a pronounced difference in the yz -plane between the two configurations. When the incident circularly polarized beam has a flat-top profile, the force is nearly central symmetric with respect to the coordinate origin and exhibits a zero value at the origin on the yz -plane, closely matching the afore-mentioned ideal requirement (Fig. 1D, left panel). In contrast, when the incident beam has a Gaussian profile, the force is radially asymmetric with respect to the coordinate origin. A pronounced imbalance along the positive and negative halves of the z -axis results in a significant downward shift of the atomic cloud centroid, while the radial force along the y -axis becomes negligible near the center of the GMOT, leading to a substantial decrease in the number of trapped atoms. By expanding the Gaussian beam, the force gets gradually close to central symmetric with respect to the coordinate origin. Notably,

when the beam is expanded to a diameter of $d = 60$ mm, the forces become comparable to that of flat-top beam configurations, thereby providing a favorable condition for atom trapping.

The above analysis shows that GMOT systems using Gaussian beams require substantial beam expansion to achieve a nearly uniform intensity profile in the central region for atom trapping. However, expanding the Gaussian beam demands significant space along its propagation path and leads to substantial laser energy waste. For instance, in the case of a Gaussian beam with a 60 mm diameter illuminating a grating chip with a 20 mm side length, only 19.93% of the beam energy is indeed utilized for atom cooling and trapping. In contrast, flat-top beams overcome the limitations of Gaussian beams by enabling near-perfect laser power utilization. Furthermore, for the same laser power applied to the grating chip, flat-top beams improve atom trapping efficiency and provide a more balanced scattering force distribution. Existing methods for generating flat-top beams, such as using axicons (35), freeform lenses (36), or liquid crystals (37), are effective but require considerable space and lack flexibility in customizing the beam size and position—both critical for tailored low-SWaP atom trapping systems. In this work, we demonstrate that a single planar optical metasurface can be engineered to generate a flat-top beam within a short propagation distance, with its size precisely tailored to the grating chip dimensions. This approach successfully resolves the space and customization limitations of conventional optical elements. Additionally, the metasurface is dual-functional: it not only shapes the Gaussian beam into a flat-top profile but also simultaneously converts its linear polarization state to circular, further eliminating the need for quarter-wave plates in conventional setups.

In a MOT-based laser cooling architecture, the atoms are cooled and trapped by the combination of optical field and magnetic field. Thus, pair of anti-Helmholtz coils are used to

form a magnetic potential well to trap the atoms, which typically consists of two identical coils (with the same radius, current, and number of turns) that carry currents in opposite directions. To achieve a magnetic field gradient of over 10 Gs/cm (a typical requirement in alkali-atom trapping systems) (38), the required coil currents grow substantially with increasing trap dimensions, creating significant heat dissipation challenges in scaled-up configurations. In this work, we propose a planar coil chip architecture that offers significantly reduced weight and volume by employing a single coplanar annular structure (Fig. 1B, bottom panel). This design incorporates multiple nested coils with varying radii, turn numbers, and current directions, optimized to achieve the desired magnetic field with minimal power consumption. This planar structure also facilitates integration with other on-chip laser cooling components, enhancing compatibility and miniaturization of the whole GMOT system.

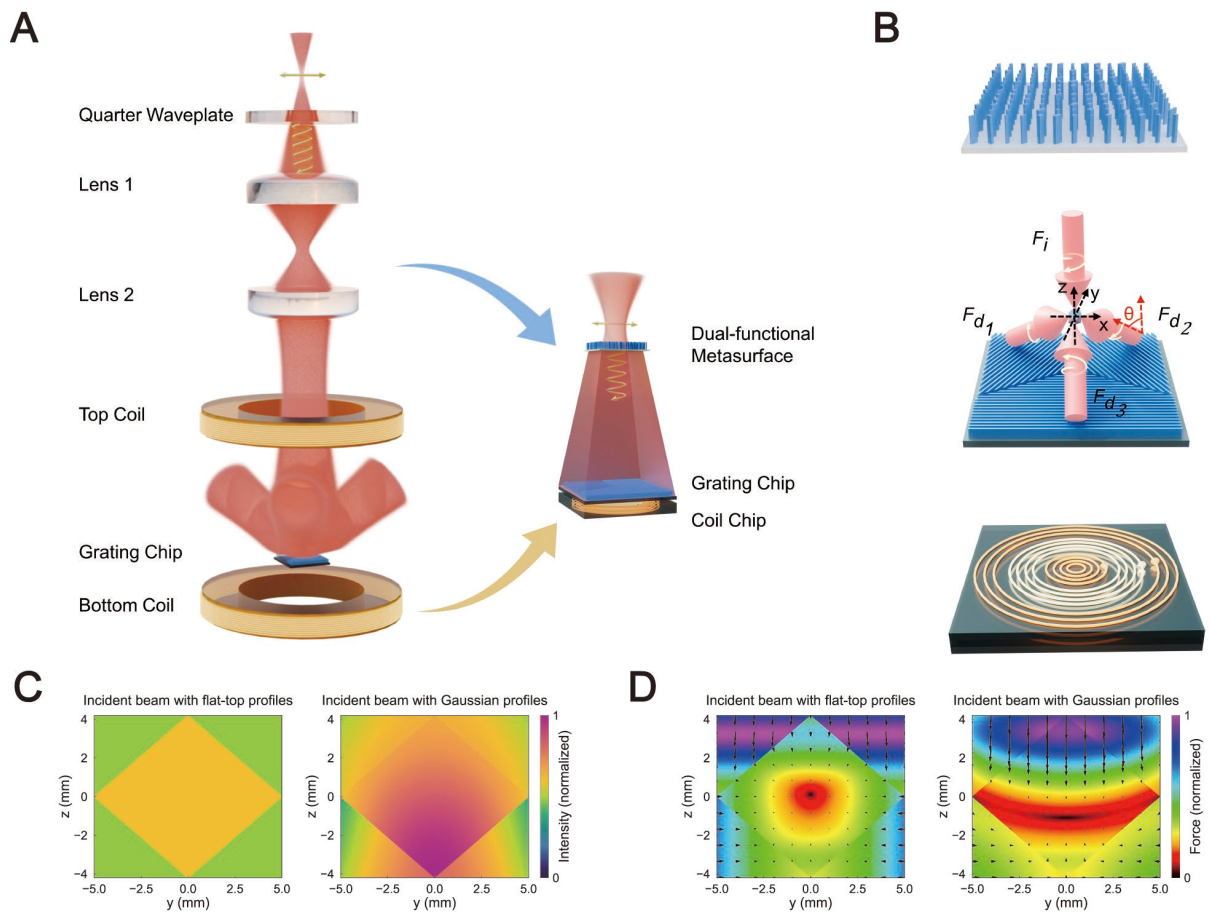


Figure 1. Transition from conventional GMOT systems to low-SWaP GMOT systems incorporating both planar optical and magnetic components. (A) Left panel: Schematic of a traditional GMOT setup utilizing conventional bulky optical and magnetic components. A linearly polarized Gaussian beam is converted to be circularly polarized by a quarter-wave plate and then expanded by a lens pair before reaching the grating chip, which comprises three linear gratings symmetrically arranged at 120° . The incident laser beam and the associated three grating-diffracted beams intersect within the vacuum cell, achieving equilibrium at the center of the quadrupole magnetic field generated by a pair of anti-Helmholtz coils. Right panel: Schematic of the proposed low-SWaP GMOT setup seamlessly integrating both a dielectric metasurface and a planar coil chip. The metasurface converts the incident linearly-polarized Gaussian beam into a circularly polarized flat-top beam, whose size precisely matches the grating chip area at a short propagation distance beyond the metasurface. The planar coil chip is employed to replace the conventional 3D anti-Helmholtz coil assembly to generate the necessary quadrupole magnetic field for atom trapping. (B) Schematic

illustration of the key components in the low-SWaP GMOT system. Top panel: the dual-functional metasurface consisting of high-aspect-ratio Si nanopillars with rectangular cross-sections. Middle panel: the Si grating chip comprising three linear gratings symmetrically arranged at 120° angles with respect to each other. Bottom panel: The planar coil chip consisting of 10 layers of nested copper circuits in a serial configuration. **(C)** Calculated spatial beam intensity distribution on the yz plane when the grating chip is illuminated by incident beams with different profiles. The total energy of the incident beam irradiated on the grating chip area is set to be the same, regardless of the beam profile or size. Left panel: when the incident beam has a flat-top profile with a side length of $L = 20$ mm matching that of the grating chip, the GMOT region exhibits a uniform spatial intensity distribution. Right panel: when the incident beam has a Gaussian profile with a diameter of $d = 20$ mm, the GMOT region exhibits a characteristic intensity decay as the radial distance from the grating chip center and the vertical height above the chip surface increase. **(D)** The theoretical scattering force, shown as vector and magnitude, on the yz plane for different illumination beams. Left panel: when the incident beam has a flat-top profile with a side length of $L = 20$ mm matching that of the grating chip, the force is nearly central symmetric with respect to the coordinate origin and exhibits a zero value at the origin. Right panel: when the incident beam has a Gaussian profile with a diameter of $d = 20$ mm, the force is radially asymmetric with respect to the coordinate origin and exhibits a serious imbalance on the positive and negative halves of the z -axis, while the radial forces become negligible along the y -axis at the center region of GMOT.

Dual-functional metasurface for simultaneous flat-top beam generation and circular polarization conversion

Here, we design a transmission-type dual-functional metasurface that transforms a linearly-polarized incident Gaussian beam into a circularly-polarized output flat-top beam (FTB), with the output beam size precisely matched to that of the grating chip (Fig. 2A). Optical metasurfaces, composed of subwavelength-scale nanostructures, offer a powerful platform for multi-dimensional light field manipulation within a planar architecture (39-51). In this study, a metasurface is implemented to simultaneously shape the wavefront and control the polarization state of the incident cooling beam, eliminating the need for separate lenses and waveplates typically required in conventional GMOT systems and thereby offering a compact and efficient beam manipulation solution. The electromagnetic (EM) response of a metasurface's constituent meta-atom can be represented by the Jones matrix:

$$J = R(-\theta)J_0(o, e)R(\theta) = \begin{bmatrix} \cos \theta & -\sin \theta \\ \sin \theta & \cos \theta \end{bmatrix} \begin{bmatrix} t_o e^{i\Delta_o} & 0 \\ 0 & t_e e^{i\Delta_e} \end{bmatrix} \begin{bmatrix} \cos \theta & \sin \theta \\ -\sin \theta & \cos \theta \end{bmatrix}. \quad (1)$$

Here, Δ_o and Δ_e are the phase shifts imparted on electric fields along the two main axes (o- and e-axis) of the meta-atom, and t_o and t_e represent the amplitude transmission coefficients of the electric fields along these two axes. θ denotes the in-plane rotation angle of the meta-atom within its unit cell. To achieve efficient linear-to-circular polarization conversion, the meta-atom needs to function similarly to a quarter-wave plate. This can be accomplished when the difference between two phase shifts Δ_o and Δ_e is close to $\pi/2$ ($\Delta = \Delta_o - \Delta_e \approx \pi/2$), and the amplitude transmission coefficients t_o and t_e are nearly unity ($t_o \approx 1$, $t_e \approx 1$). In the case where the incident light is linearly polarized along the x -axis ($E_{in} = [1, 0]^T$) and the output light is designed to be left-handed circularly polarized (LCP), the polarization direction

of the incident light should make an angle of 45° with respect to the long axis of the meta-atom ($\theta = 45^\circ$). The output electrical field can be represented as:

$$\begin{aligned} E_{out} &= JE_{in} \\ &= e^{i\Delta_o} R(-45^\circ) \begin{bmatrix} 1 & 0 \\ 0 & -i \end{bmatrix} R(45^\circ) \begin{bmatrix} 1 \\ 0 \end{bmatrix} \\ &= \frac{(1+i)e^{i\Delta_o}}{2} \begin{bmatrix} 1 \\ i \end{bmatrix}. \end{aligned} \quad (2)$$

It can be observed that the phase of the output LCP light is closely related to the phase shift Δ_o provided by a given meta-atom. By adjusting the structural parameters of the meta-atoms to provide the required Δ_o values at different positions across the metasurface plane, an on-demand phase modulation profile can be readily implemented.

In this study, an incident Gaussian beam is modulated by a square-shaped metasurface and subsequently transformed into an FTB at a pre-set propagation distance beyond the metasurface. Based on the energy mapping principle, we derive the phase modulation profile $\phi(x_0, y_0)$ of the metasurface.

$$\phi(x_0, y_0) = \phi_x(x_0) + \phi_y(y_0), \quad (3)$$

$$\phi_x(x_0) = \int_0^{x_0} \frac{2\pi}{\lambda} \frac{1}{\sqrt{1 + \frac{z_0^2}{\left[\frac{\frac{L_x}{2} \operatorname{erf}\left(\frac{\sqrt{2}x}{w_i}\right)}{\operatorname{erf}\left(\frac{\sqrt{2}D_0}{2w_i}\right)} - x \right]^2}}} dx, \quad (4)$$

$$\phi_y(y_0) = \int_0^{y_0} \frac{2\pi}{\lambda} \frac{1}{\sqrt{1 + \frac{z_0^2}{\left[\frac{\frac{L_y}{2} \operatorname{erf}\left(\frac{\sqrt{2}y}{w_i}\right)}{\operatorname{erf}\left(\frac{\sqrt{2}D_0}{2w_i}\right)} - y \right]^2}}} dy. \quad (5)$$

Here, z_0 is the propagation distance beyond the metasurface where the target FTB is formed.

λ is the free-space wavelength of the cooling light, w_i is the waist radius of the incident Gaussian beam, and D_0 is the side length of the square-shaped metasurface. L_x and L_y denote the side lengths of the rectangular-shaped FTB along the x - and y -axes, respectively. In general, the FTB can have different sizes along the x - and y -axes. In this work, the FTB is designed to match the square-shaped grating chip, making it have the same square shape with side length $L_x = L_y = L$. The term “erf” denotes the error function, defined as $\text{erf}(q) = \frac{2}{\sqrt{\pi}} \int_0^q \exp(-t^2) dt$.

For the constructed GMOT system, the output Gaussian beam from the laser source has a free-space wavelength of $\lambda = 780$ nm (for cooling ^{87}Rb atoms) and a waist radius of $w_i = 250$ μm . The size of the generated FTB is designed to match the dimensions of the grating chip, with a corresponding side length of $L = 20$ mm. Moreover, the propagation distance for FTB formation is set as $z_0 = 10$ cm, which ensures both a compact GMOT system footprint and high beam performance. To fully utilize the incident laser energy, the metasurface is designed to have a side length of $D_0 = 1.5$ mm, three times larger than the incident Gaussian beam diameter. Using these parameters, the phase modulation profile $\phi(x_o, y_o)$ is derived and plotted in Fig. 2B. For the final metasurface design, an additional gradient phase $\phi_g = \frac{2\pi}{\lambda} x_o \sin \alpha$ is introduced, causing an $\alpha = 8^\circ$ tilt of the FTB along the x_o -axis. This phase modification effectively separates the generated FTB from the directly-transmitted residual beam, ensuring high beam purity and facilitating easier observation and measurement.

To implement the designed dual-functional metasurface, amorphous silicon (a-Si), which exhibits high refractive index and low absorption coefficient at the device’s operational wavelength, is chosen as the metasurface’s constituent material. Each a-Si meta-atom acts as a miniaturized quarter-wave plate for linear-to-circular polarization conversion, and at the same

time, the phase of the transmitted circularly polarized light is controlled by the meta-atom's dimensions. To determine the structural parameters of the a-Si meta-atoms, the amplitude transmittance and phase shift for propagation of $\lambda = 780$ nm light, linearly-polarized either (i) parallel to the major axis (t_o and Δ_o), or (ii) parallel to the minor axis (t_e and Δ_e) of the rectangular a-Si nanopillar are computed using Finite-Difference Time-Domain (FDTD) simulations with periodic boundary conditions. For a chosen pillar height $H = 1000$ nm and lattice spacing $P = 350$ nm, the major and minor axis lengths of the pillar, L_o and L_e , are iteratively varied to identify orthogonal principal axis combinations simultaneously leading to $\Delta_o - \Delta_e \approx \pi/2$ and $t_o \approx t_e$, in other words, quarter-waveplate-like operation. To facilitate the above parameter searching process, a figure-of-merit (FoM) function is defined as $\text{FoM} = \log_{10} \left(\left| \frac{t_o}{t_e} e^{i(\Delta_o - \Delta_e)} - e^{i\pi/2} \right| \right)$ and displayed in Fig. 2C. The blue-colored regions (i.e., low-FoM value regions) correspond to various combinations of L_o and L_e that satisfy the target quarter-waveplate-like operation. Through this process, 1212 a-Si nanopillars with different orthogonal principal axis combinations are selected, providing a full 0 to 2π phase shift ϕ coverage with phase intervals down to 0.0268 radians. These nanopillars also exhibit high linear-to-circular polarization conversion efficiency η exceeding 80%, and a low root-mean-square (RMS) efficiency variation of 4.2% (Fig. 2D). Finally, the dual-functional metasurface is constructed by mapping the target phase modulation profile to the obtained meta-atom library.

The metasurface fabrication process comprises several key steps, including a-Si film deposition via plasma-enhanced chemical vapor deposition (PECVD) on fused silica substrate, electron beam lithography (EBL), aluminum (Al) etching mask lift-off, and inductively coupled plasma reactive ion etching (ICP-RIE). A detailed description of the fabrication process is provided in the Materials and Methods section. The fabricated square-shaped metasurface has

a side length of 1.5 mm and visually exhibits uniform color with minimal defects (Fig. 2E, left panel). Scanning electron microscope images (Fig. 2E, right panel) show high-aspect-ratio (up to 14:1) a-Si nanopillars with well-defined rectangular cross-sections and smooth sidewalls.

To characterize the performance of the fabricated metasurface, the device is positioned at the beam waist of the Gaussian beam from the laser source. The intensity profile and polarization state of the transmitted FTB are recorded using a complementary metal-oxide semiconductor (CMOS) camera and a near-infrared polarimeter, respectively. Figure 2F shows the intensity profiles of the generated FTB at different propagation distances beyond the metasurface ($z_0 = 6, 8, 10, 12,$ and 14 cm). As the propagation distance increases, the size of the FTB gradually expands, and the beam edges become sharper. Figure 2G displays the cross-sectional cut of the intensity profile of the FTB at the designed propagation distance of $z_0 = 10$ cm, where the grating chip will be positioned. To access the quality of the generated FTB, two parameters are defined: the flatness factor $F = \frac{I_{average}}{I_{maximum}}$ and the root-mean-squared (RMS) intensity variation $\delta = \sqrt{\frac{\sum_{i=1}^n (I_i - I_{average})^2}{n}}$ (52). Here, $I_{average}$ and $I_{maximum}$ are the average and maximum intensity values in the 2D cross-section of the FTB, respectively. I_i is the intensity of the sampling point i and $n = 4.94 \times 10^6$ is the total number of sampling points in the beam's 2D cross-section. At the designed propagation distance, the square-shaped FTB exhibits a flatness factor $F = 78.58\%$ and an RMS intensity variation $\delta = 0.08$. The device not only achieves comparable RMS intensity variation to existing solutions (36, 37, 53), but also enables an almost perfect linear-to-circular polarization conversion. The measured polarization states of the incident linearly polarized Gaussian beam and the transmitted circularly polarized FTB are mapped on the Poincaré sphere (Fig. 2H). The degree of circular

polarization (DOCP), which evaluates the metasurface's polarization conversion capability, is measured to be 98.64%. The metasurface's operational efficiency, defined as the ratio between the intensity of the FTB at the target propagation distance and the intensity of the incident Gaussian beam, is measured to be 42.01%.

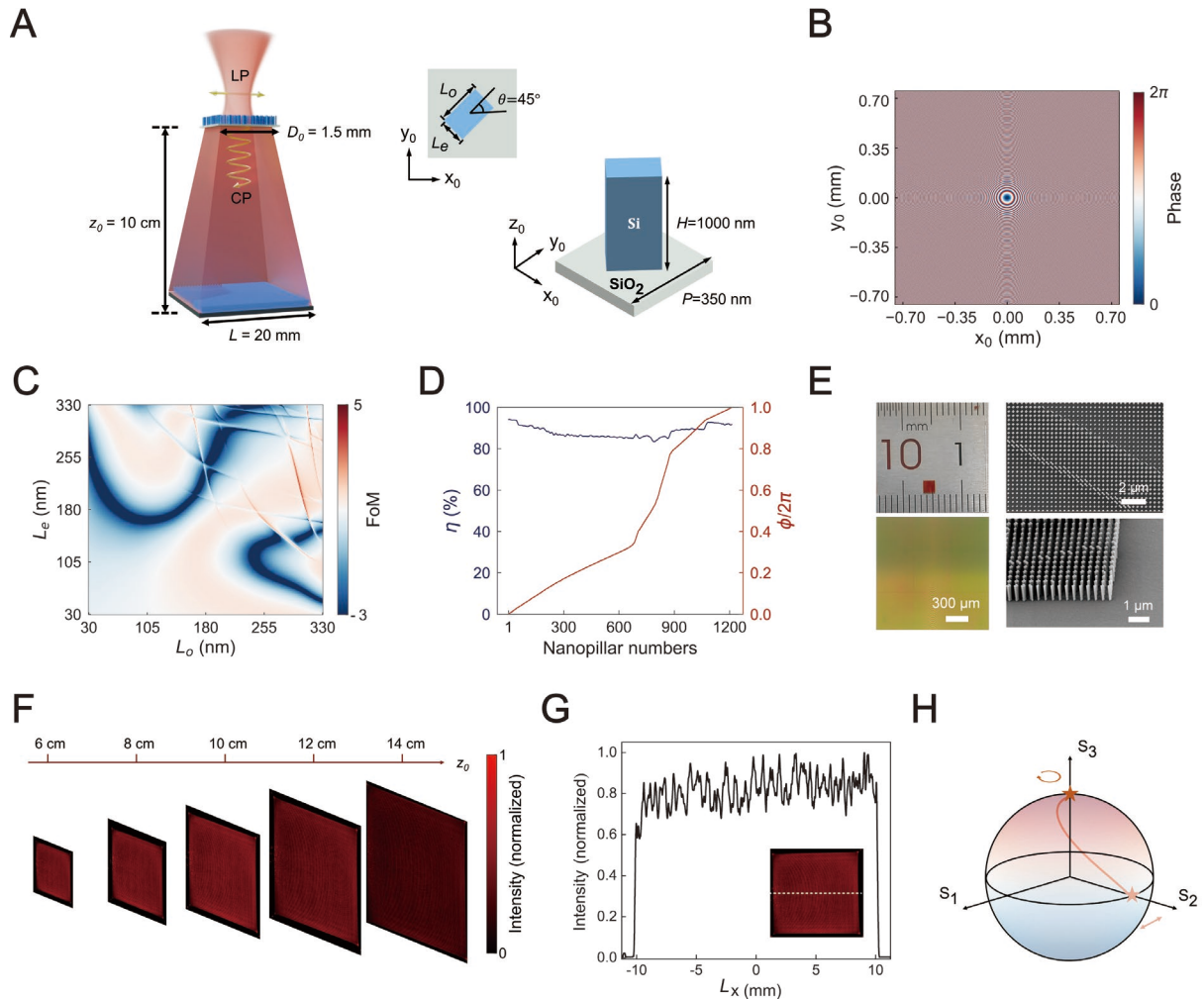


Figure 2. Dual-functional metasurface for simultaneous flat-top beam generation and linear-to-circular polarization conversion. (A) Schematic of the transmission-type metasurface that transforms an incident linearly-polarized Gaussian beam into a circularly-polarized flat-top beam whose size precisely matches that of the grating chip. Inset: Perspective and top views of the metasurface unit-cell, consisting of an amorphous Si nanopillar with a rectangular cross-section (side lengths of L_o and L_e) and rotation angle $\theta = 45^\circ$ arranged on a SiO_2 substrate to form a square lattice with subwavelength lattice spacing P . Each meta-atom functions like a quarter-wave plate to realize linear-to-circular

polarization conversion. By varying side lengths L_o and L_e as a function of the nanopillar position across the metasurface device, phase modulation is imparted on the transmitted circularly polarized light to form the target FTB. **(B)** Phase modulation profile of the metasurface (with a side length $D_0 = 1.5$ mm) designed to shape a circularly-shaped Gaussian beam (with a waist diameter of $500 \mu\text{m}$) into a square-shaped FTB (with a side length of 20 mm) at a working distance $z_0 = 10$ cm beyond the metasurface. **(C)** Quarter-waveplate figure of merit (FoM) versus nanopillar in-plane dimensions (L_o and L_e) at the target free-space wavelength $\lambda = 780$ nm, where the blue-colored regions (i.e., low-FoM value regions) correspond to various combinations of L_o and L_e that satisfy the quarter-waveplate-like operation criteria. **(D)** Linear-to-circular polarization conversion efficiency η and phase shift ϕ of the transmitted circularly polarized light for the selected 1212 nanopillars. **(E)** Left panel: Photo (upper image) and optical micrograph (lower image) of the fabricated metasurface. Right panel: Top view and oblique view (viewing angle: 49°) SEM images showing the details of constituent rectangular Si nanopillars. **(F)** Normalized intensity profiles of the generated FTB at propagation distances of $z_0 = 6, 8, 10, 12,$ and 14 cm beyond the metasurface. As the propagation distance increases, the FTB gradually expands and its edges become sharper. **(G)** Cross-sectional cut of the intensity profile of the FTB at the designated working distance ($z_0 = 10$ cm), where the grating chip is positioned. Inset: Measured two-dimensional intensity profiles of the FTB. The dashed white line indicates the sampling direction for the cross-sectional cut. **(H)** Polarization states of the incident linearly polarized Gaussian beam and the transmitted circularly polarized FTB mapped onto the Poincaré sphere (denoted by stars). The degree of circular polarization (DOCP) is measured to be 98.64% .

Planar coil chip for miniaturized magnetic field generation

The detailed schematic of the planar coil chip we develop is shown in Fig. 3A. This planar design integrates the functionality of a conventional coil pair into a single coplanar annular structure, and employs multiple coil groups patterned onto a printed circuit board (PCB) with counter-flowing currents. The simple architecture and straightforward fabrication process of this coil chip enable it to readily replace conventional anti-Helmholtz coils, facilitating planarization of all core components in the GMOT system. The chip generates a null magnetic field with sufficient gradient, coinciding spatially with the point where the incident light and grating-generated diffracted light fields overlap. The chip comprises multiple nested coils with varying radii, turn numbers, and current directions, all connected in series and driven by the same current I . By carefully selecting and optimizing these parameters, the structure can generate the desired magnetic field with high precision. Moreover, the atom trapping position is flexibly tunable to a defined distance above the chip, enabling a more compact system configuration. To further enhance magnetic field generation efficiency while minimizing power consumption and heat accumulation, the chip is designed to incorporate multiple vertically stacked layers of coplanar annular coils in a serial configuration.

For the MOT to function properly, the quadrupole magnetic field needs to exhibit a zero value at the laser beam intersection point, and at the same time, maintain a spatial gradient of approximately 12 Gs/cm. The strength and spatial gradient of the magnetic field generated by a planar coil chip at a given point on the z -axis are calculated as:

$$B_z(0,0,z) = \frac{\mu_0}{2} \left(\pm \frac{N_1 R_1^2 I_0}{(R_1^2 + z^2)^{\frac{3}{2}}} \pm \frac{N_2 R_2^2 I_0}{(R_2^2 + z^2)^{\frac{3}{2}}} \cdots \pm \frac{N_n R_n^2 I_0}{(R_n^2 + z^2)^{\frac{3}{2}}} \right), \quad (6)$$

$$\frac{\partial B_z}{\partial z}(0,0,z) = \frac{3\mu_0 z_0}{2} \left(\pm \frac{N_1 R_1^2 I_0}{(R_1^2 + z^2)^{\frac{5}{2}}} \pm \frac{N_2 R_2^2 I_0}{(R_2^2 + z^2)^{\frac{5}{2}}} \cdots \pm \frac{N_n R_n^2 I_0}{(R_n^2 + z^2)^{\frac{5}{2}}} \right). \quad (7)$$

Here, μ_0 is the magnetic permeability in vacuum. I_0 is the current applied to the series-connected planar coils. N_i and R_i represent the number of turns and radius of the i -th nested coil, respectively. The “+” symbol denotes counter-clockwise coil current flow, while “-” indicates clockwise flow. n is the total number of nested coils. In this study, the operating point is chosen as $(0, 0, z = 6.5 \text{ mm})$. By carefully designing these parameters, we can achieve the target magnetic field with a strength $B_z(0, 0, z = 6.5 \text{ mm}) = 0$ and spatial gradient $\frac{\partial B_z}{\partial z}(0, 0, z = 6.5 \text{ mm}) \approx 12 \text{ G/cm}$ at the operating point.

We fabricate the designed coil chip comprising 10 layers of coplanar annular coil structures by depositing copper wires onto the surface of a printed circuit board (PCB). Each layer is 70 μm thick, with a wire width of 545 μm and a spacing of 150 μm between adjacent wires. Each layer is composed of three groups of nested coils, separated from each other by an insulating layer (Fig. 3B). The innermost coil has $N_1 = 1$ turn with a radius of 1.4 mm. The middle coil comprises $N_2 = 13$ turns with radii ranging from 2.095 mm to 10.435 mm. The outermost coil includes $N_3 = 11$ turns with radii spanning from 11.13 mm to 18.08 mm. Figure 3C shows images of a conventional anti-Helmholtz coil (left) and the developed planar coil chip (right), both capable of generating comparable magnetic field gradients. In contrast to the bulky traditional coil, the planar chip has a total thickness of just 2 mm and a footprint of $39 \times 39 \text{ mm}$ —representing a reduction in volume by orders of magnitude. In addition, the weight of the chip is only 8.95 g, more than 100 times lighter than the conventional anti-Helmholtz coil. Figure 3D displays the simulated magnetic field distribution of this coil chip structure, showing the magnetic field pattern on the yz plane (perpendicular to the coil plane)

under a driving current of $I = 2.2$ A. At a height of $z = 6.5$ mm, the magnetic field strength approaches 0 Gs, with a gradient reaching 11.86 Gs/cm.

The performance of the chip is experimentally evaluated. The strength of the magnetic field at different heights from the coil center, under an applied current of 2.2 A, is measured by a magnetometer with a step size of 0.5 mm along the z direction (Fig. 3E). The chip generates a zero-strength magnetic field at a height of 6.5 mm above the chip, with a field gradient of 11.7 Gs/cm along the z -axis. By varying the coil's operating current, the corresponding power consumption can be calculated. Figure 3F presents the experimental result of the power consumption of the chip versus the magnetic field gradient. As the coil power increases, the spatial gradient of the magnetic field at the operating point (where the magnetic field strength equals zero) gradually becomes larger. The power consumption, when the field gradient is 11.7 Gs/cm at the operating point, is calculated to be 0.56 W. As a comparison, conventional anti-Helmholtz coils typically consume several tens of watts of power for realizing similar field gradients (38). These results demonstrate that the planar coil chip meets the steady-state magnetic field gradient and power consumption requirements for energy-efficient MOT systems.

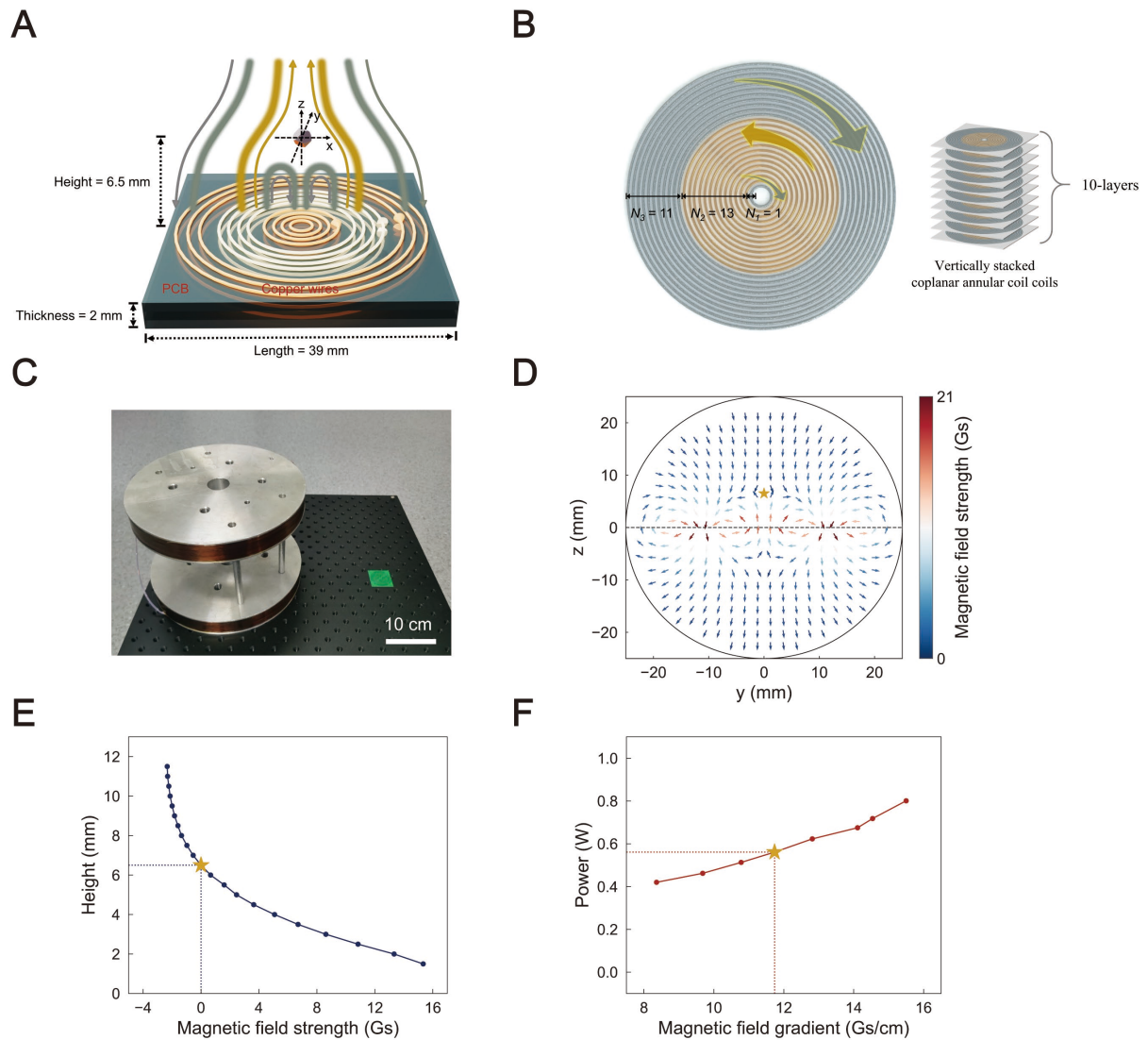


Figure 3. Miniaturized magnetic field generation based on a planar coil chip. (A) Schematic of the multilayer planar coil chip designed to generate the quadrupole magnetic field. The structure consists of multiple nested annular coils connected in series and carrying the same current I , with each coil exhibiting different radii, turn counts, and current directions. By carefully selecting the number of nested coils and optimizing their parameters, the desired quadrupole magnetic field can be accurately generated. This configuration allows flexible positioning of the atom trapping region at a specified distance from the coil (a height of 6.5 mm in this case), facilitating the realization of compact cold atom systems. The implemented coil chip in this study has an overall thickness of 2 mm and a footprint of 39×39 mm. Moreover, 10 layers of vertically-stacked coplanar annular coil structures are incorporated in the chip to enhance magnetic field generation efficiency while minimizing power consumption and heat

accumulation. **(B)** Structural scheme of the multilayer planar coil chip. The chip is fabricated by depositing copper wires onto a printed circuit board (PCB) to form 10 layers of coplanar annular coil structures. Each layer is 70 μm thick, with a wire width of 545 μm and a spacing of 150 μm between adjacent wires. Every layer comprises three groups of nested coils: the innermost coil ($N_1 = 1$ turn, radius = 1.4 mm), the middle coil ($N_2 = 13$ turns, radii ranging from 2.095 mm to 10.435 mm), and the outermost coil ($N_3 = 11$ turns, radii ranging from 11.13 mm to 18.08 mm). Insert: the schematic of multiple vertically stacked layers of coplanar annular coils in a serial configuration. **(C)** Photograph comparing a conventional anti-Helmholtz coil (left, 1174.94 g) and the developed planar coil chip (right, 8.95 g). **(D)** Simulated magnetic field distribution on the yz plane at a working current of 2.2 A. The arrow directions indicate the orientation of the magnetic field, while the color scale represents the field strength. At the operating point (marked by the yellow star), the magnetic field strength approaches 0 Gs, with a gradient of 11.7 Gs/cm. **(E)** Measured magnetic field strength at different heights from the coil center, under an applied current of 2.2 A. Measurements taken along the z -direction reveal that the field strength becomes zero at a height of 6.5 mm (indicated by the yellow star), with a spatial gradient of 11.7 Gs/cm. **(F)** Measured power consumption versus the magnetic field gradient at the zero-field point. As the coil power increases, the magnetic field gradient correspondingly increases. Under the operating condition with an 11.7 Gs/cm gradient, the power consumption is 0.56 W.

Low-SWaP GMOT system incorporating both the planar optical and magnetic components

The constructed GMOT experimental setup for laser cooling and trapping of ^{87}Rb atoms is illustrated in Fig. 4A. The 780 nm cooling laser is frequency-stabilized to the $5S_{1/2} (F = 2) \rightarrow 5P_{3/2} (F' = 3)$ cycling transition on the D_2 line of ^{87}Rb atoms using the modulation transfer spectrum (MTS). A 795 nm repumping laser is locked onto the $5S_{1/2} (F = 1) \rightarrow 5P_{3/2} (F' = 2)$ transition of ^{87}Rb atoms by the saturated absorption spectrum (SAS). Both linearly-polarized laser beams are coupled into a polarization-maintaining fiber and subsequently out-coupled into free space by a fiber collimator. The dual-functional metasurface reshapes the linearly polarized output Gaussian beam into a square-shaped FTB which subsequently illuminates the planar grating chip. The FTB, together with three reflective beams diffracted by the planar grating chip, form an overlapping region in the vacuum cell. The planar coil chip is positioned beneath the grating, with its center aligned vertically with the overlapping beam region. Ultimately, the ^{87}Rb atoms are cooled and trapped within the overlapping beam region, located approximately 6.5 mm above the coil chip.

We will now investigate the unique advantages of illuminating the grating chip with a beam having a flat-top intensity profile. As demonstrated by the theoretical analysis in the earlier text, such illumination configuration provides more balanced optical forces on the cold atoms. In the experiment, the trapping performances of the two illumination beams with different profiles are compared: a flat-top profile with a side length $L = 20$ mm matching that of the grating chip, and a Gaussian profile with varying cross-sectional diameters of $d = 40$ mm, 50 mm, and 60 mm. In the case of Gaussian beam illumination, a convex lens pair is used to expand the Gaussian beam from the fiber collimator to diameters of 40, 50, and 60 mm. The

effect of atom trapping can be observed from the experimentally measured fluorescence images of the trapped atom cluster (54). When the intensity distribution of the beam illuminating the grating chip is set to a flat-top profile, the trapped atom cluster exhibits a circular shape (Fig. 4B, top panel), in contrast to the flattened shape observed when the beam has a Gaussian profile (Fig. 4B, bottom panel). As the laser power increases, significant differences are observed in the growth trends of the number of trapped atoms between the two cases. For the case of FTB illumination, the number of trapped cold atoms increases linearly with laser power, reaching a maximum of $(8.15 \pm 0.15) \times 10^6$ atoms at an incident laser power of 100 mW (Fig. 4C, red curve). The cited uncertainty represents one standard deviation of the measured data. This follows the typical trend observed in atom number variation under low atomic transitions (55). The afore-mentioned laser power corresponds to the maximum output from the employed laser system. With even higher laser powers, the number of trapped atoms is expected to continue to rise before eventually plateauing due to the saturation of atomic transitions. In sharp contrast, for the case of Gaussian beam illumination, the number of trapped atoms only increases slightly with laser power before plateauing. As the diameter of the expanded Gaussian beam increases, more atoms can be trapped at the same power level due to the more uniform intensity distribution over the grating area and thus better atom trapping efficiency. But still, the trapped atom numbers for all three Gaussian beams are consistently lower than that of the FTB under the same level of illumination laser power. As an example, the numbers of trapped atoms at the laser power of 100 mW are measured to be $(2.30 \pm 0.31) \times 10^6$, $(3.91 \pm 0.12) \times 10^6$, and $(4.23 \pm 0.13) \times 10^6$ respectively for the Gaussian beams having diameters of 40 mm, 50 mm, and 60 mm, which are all significantly lower than that of the FTB. The cited uncertainties represent one standard deviation of the measured data.

Additionally, we characterize the performance of the constructed GMOT system by examining the influence of several tunable parameters, including the detuning of the laser cooling beam and the power applied to the planar coil. With the FTB beam illuminating the grating chip at an incident power of 100 mW, the measured number of trapped cold atoms as a function of laser detuning is displayed in Fig. 4D. A detuning of approximately 8.4 MHz maximizes the number of trapped cold atoms. At this optimal detuning, the coil chip consumes only 0.56 W to generate the operating-point field gradient of 11.7 Gs/cm—over two orders of magnitude lower than the 67 W required by conventional coils. The number of trapped cold atoms gradually increases as the power applied to the planar coil rises, with an expected saturation near 10^7 atoms (Fig. 4E).

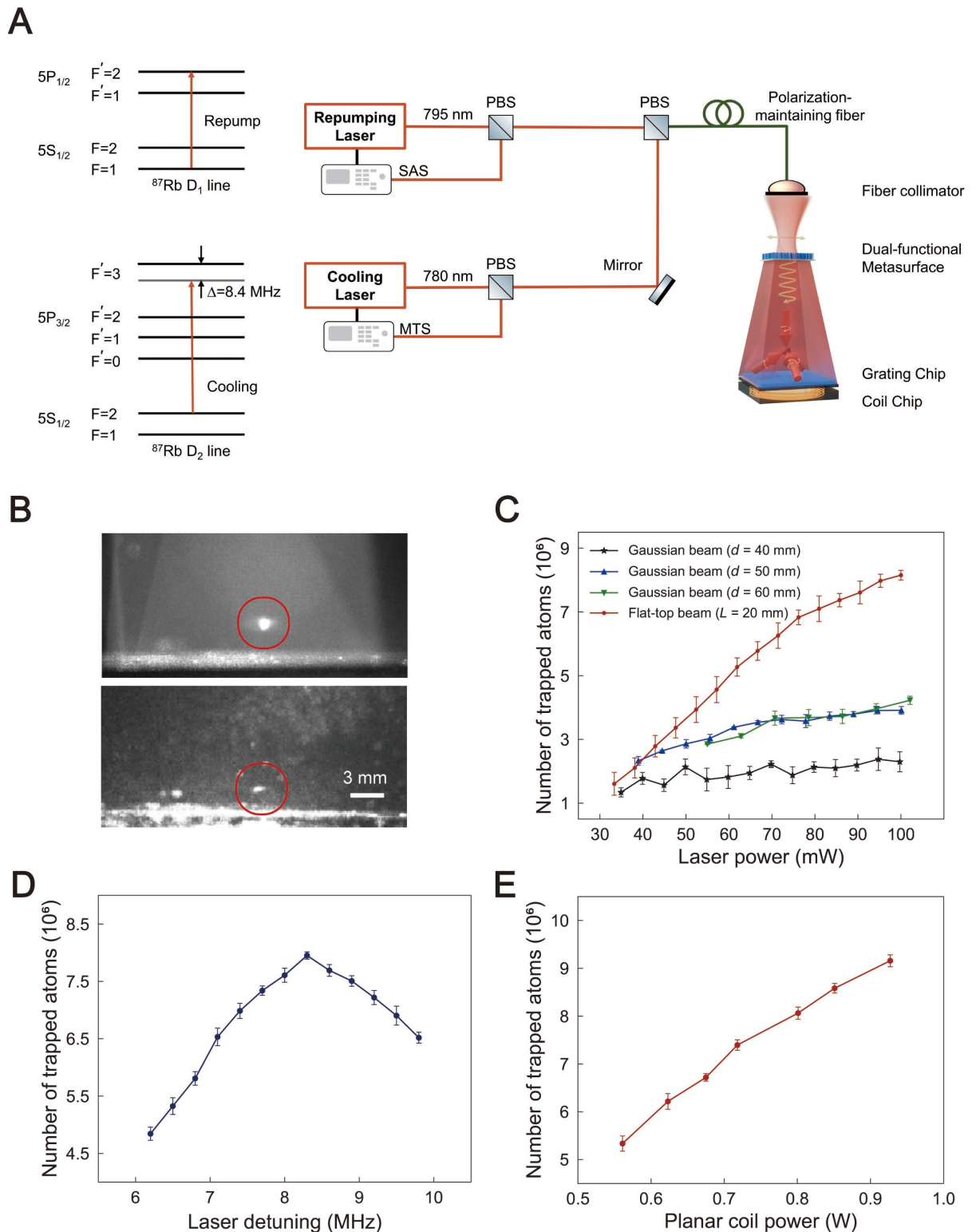


Figure 4. Experimental characterization of the Low-SWaP GMOT system incorporating both planar optical and magnetic components for cooling and trapping of ^{87}Rb atoms. (A) Schematic of

energy levels of ^{87}Rb atoms and the laser cooling setup. On the left is the D₁ and D₂ line of ^{87}Rb , respectively. The 780 nm cooling laser is tuned to the $5S_{1/2}(F=2) \rightarrow 5P_{3/2}(F'=3)$ cycling transition on the D₂ line, and the repumping laser is resonant with the $5S_{1/2}(F=1) \rightarrow 5P_{3/2}(F'=2)$ transition. On the right is the schematic illustration of the cooling setup, the cooling light is locked with the modulation transfer spectrum (MTS) technique, and the repump light is stabilized with saturated absorption spectrum (SAS) of ^{87}Rb . Both linearly-polarized laser beams are coupled into a polarization-maintaining fiber and subsequently out-coupled into free space by a fiber collimator. **(B)** Fluorescence images of trapped cold atoms under different illumination conditions. Upper panel: When an FTB with a 20 mm side length (matched to the grating chip) is used, the trapped atom cluster exhibits a circular shape. Lower panel: When a Gaussian beam (expanded to a diameter of 50 mm) is used, the trapped atom cluster displays a flattened shape. **(C)** Measured number of trapped cold atoms versus laser power for the cases of FTB and expanded Gaussian beam illuminations. Under FTB illumination, the trapped atom number increases linearly with laser power, reaching up to $(8.15 \pm 0.15) \times 10^6$ atoms at a peak power of 100 mW. In contrast, Gaussian beam illumination results in a modest increase that quickly plateaus, with trapped atom numbers significantly lower than that achieved with the FTB at the same level of laser power, reaching up to $(2.30 \pm 0.31) \times 10^6$, $(3.91 \pm 0.12) \times 10^6$, and $(4.23 \pm 0.13) \times 10^6$ respectively for the Gaussian beam diameters of 40 mm, 50 mm, and 60 mm at a peak power of a 100 mW. The cited uncertainties represent one standard deviation of the measured data. **(D)** Measured number of trapped cold atoms as a function of laser detuning under FTB illumination at the peak power of 100 mW. The maximum atom number is observed at a detuning of approximately 8.4 MHz. **(E)** Measured number of trapped cold atoms as a function of planar coil power at the optimal detuning. The trapped atom number gradually increases with the power applied to the planar coil, with an expected saturation near 10^7 atoms. Error bars denote one standard deviations of the measured data in Figs. **C**, **D**, and **E**.

Conclusion

In summary, we have developed a fully planar, chip-based cold atom platform with significantly reduced system size, weight, and power consumption, by replacing conventional bulky optical and magnetic components with a dielectric dual-functional metasurface and a planar multi-layer coil chip. The metasurface efficiently transforms a linearly polarized Gaussian beam into a circularly polarized flat-top beam, achieving both high intensity uniformity and degree of circular polarization. Meanwhile, the planar coil chip reliably generates the required quadrupole magnetic field gradient for effective atom trapping. Experimental results demonstrate that the platform can trap up to 8×10^6 ^{87}Rb atoms, achieving superior trapping efficiency over setups using expanded Gaussian beams with a range of beam diameters. The seamless integration of both planar metasurface optics and planar magnetic components represents a major step toward the miniaturization of cold atom systems. Moreover, as atomic clocks and quantum sensors often require additional components to enhance signal-to-noise ratios (56-59)—adding system complexity and power demands—this on-chip integration strategy offers a compelling balance of performance, simplicity, and scalability. The proposed platform provides a foundation for the development of miniaturized and energy-efficient quantum technologies, enabling new possibilities for quantum sensing and precision measurement in field-deployable and resource-constrained environments such as compact atomic clocks, portable quantum sensors, and spacecraft-based quantum instruments.

Materials and Methods

Metasurface fabrication

The metasurface fabrication process begins with the deposition of 1000-nm-thick amorphous silicon (a-Si) layer onto fused silica substrate using plasma-enhanced chemical vapor deposition (PECVD). The film's refractive index and thickness value are characterized by reflection-mode spectroscopic ellipsometry using the interference enhancement method (60), at three different angles of incidence (55° , 65° , and 75°) with respect to the normal to the plane of the a-Si layer. Electron beam (e-beam) lithography is employed to expose the metasurface pattern on a layer of positive-tone e-beam resist. After resist development, a 40-nm-thick aluminum (Al) layer is deposited onto the exposed resist, and a lift-off process is used to transfer the metasurface pattern onto the Al layer, forming a hard mask for the subsequent Si etching. The metasurface pattern is then transferred from the Al layer to the Si layer using an inductively coupled plasma reactive ion etching (ICP-RIE) process. Finally, the array of Si nanopillars is obtained by removing the Al hard mask and cleaning the sample using solvent.

Acknowledgement

The authors would like to acknowledge the support by the National Key Research and Development Program of China under Grant No. 2024YFB2809200, the National Natural Science Foundation of China under Grant Nos. 62205113, 62075078, 62135004, and 12273087, and the Natural Science Foundation of Hubei Province under Grant No. 2024AFA071.

Reference

1. A. Ashkin, J. P. Gordon, Cooling and trapping of atoms by resonance radiation pressure. *Opt. Lett.* **4**, 161-163 (1979).
2. S. Chu, L. Hollberg, J. E. Bjorkholm, A. Cable, A. Ashkin, Three-dimensional viscous confinement and cooling of atoms by resonance radiation pressure. *Phys. Rev. Lett.* **55**, 48-51 (1985).
3. S. Chu, Cold atoms and quantum control. *Nature* **416**, 206-210 (2002).
4. Z. Zhang, K. J. Arnold, R. Kaewuam, M. D. Barrett, $^{176}\text{Lu}^+$ clock comparison at the 10^{-18} level via correlation spectroscopy. *Sci. Adv.* **9**, 1971 (2023).
5. J. Li, X. Cui, Z. Jia, D. Kong, H. Yu, X. Zhu, X. Liu, D. Wang, X. Zhang, X. Huang, M. Zhu, Y. Yang, Y. Hu, X. Liu, X. Zhai, P. Liu, X. Jiang, P. Xu, H. Dai, Y. Chen, J. Pan, A strontium lattice clock with both stability and uncertainty below 5×10^{-18} . *Metrologia* **61**, 015006 (2024).
6. J. C. Halimeh, M. Aidelsburger, F. Grusdt, P. Hauke, B. Yang, Cold-atom quantum simulators of gauge theories. *Nat. Phys.* **21**, 25-36 (2025).
7. J. Ye, P. Zoller, Essay: Quantum sensing with atomic, molecular, and optical platforms for fundamental physics. *Phys. Rev. Lett.* **132**, 190001 (2024).
8. P. D. Lett, R. N. Watts, C. I. Westbrook, W. D. Phillips, P. L. Gould, H. J. Metcalf, Observation of atoms laser cooled below the doppler limit. *Phys. Rev. Lett.* **61**, 169-172 (1988).
9. D. Frese, B. Ueberholz, S. Kuhr, W. Alt, D. Schrader, V. Gomer, D. Meschede, Single atoms in an optical dipole trap: Towards a deterministic source of cold atoms. *Phys. Rev. Lett.* **85**, 3777-3780 (2000).
10. D. Jaksch, C. Bruder, J. I. Cirac, C. W. Gardiner, P. Zoller, Cold bosonic atoms in optical lattices. *Phys. Rev. Lett.* **81**, 3108-3111 (1998).
11. E. L. Raab, M. Prentiss, A. Cable, S. Chu, D. E. Pritchard, Trapping of neutral sodium atoms with radiation pressure. *Phys. Rev. Lett.* **59**, 2631-2634 (1987).
12. A. L. Collopy, S. Ding, Y. Wu, I. A. Finneran, L. Anderegg, B. L. Augenbraun, J. M. Doyle, J. Ye, 3D magneto-optical trap of yttrium monoxide. *Phys. Rev. Lett.* **121**, 213201 (2018).
13. Z. Zeng, S. Deng, S. Yang, B. Yan, Three-dimensional magneto-optical trapping of barium monofluoride. *Phys. Rev. Lett.* **133**, 143404 (2024).
14. X. Wu, F. Zi, J. Dudley, R. J. Bilotta, P. Canoza, H. Müller, Multiaxis atom interferometry with a single-diode laser and a pyramidal magneto-optical trap. *Optica* **4**, 1545-1551 (2017).
15. W. Bowden, R. Hobson, I. R. Hill, A. Vianello, M. Schioppo, A. Silva, H. S. Margolis, P. E. G. Baird, P. Gill, A pyramid mot with integrated optical cavities as a cold atom platform for an optical lattice clock. *Sci. Rep.* **9**, 11704 (2019).
16. Z. Yu, Y. Zhu, M. Yao, F. Qi, L. Chen, C. Zou, J. Duan, X. Liu, Low power consumption grating magneto-optical trap based on planar elements. *Opt. Express* **32**, 8919-8928 (2024).
17. L. Chen, C. Huang, X. Xu, Y. Zhang, D. Ma, Z. Lu, Z. Wang, G. Chen, J. Zhang, H. X. Tang, C. Dong, W. Liu, G. Xiang, G. Guo, C. Zou, Planar-integrated magneto-optical trap. *Phys. Rev. Appl.* **17**, 034031 (2022).
18. S. A. Bondza, T. Leopold, R. Schwarz, C. Lisdat, Achromatic, planar fresnel-reflector for a single-beam magneto-optical trap. *Rev. Sci. Instrum.* **95**, 013202 (2024).
19. A. Isichenko, N. Chauhan, D. Bose, J. Wang, P. D. Kunz, D. J. Blumenthal, Photonic integrated beam delivery for a rubidium 3D magneto-optical trap. *Nat. Commun.* **14**, 3080 (2023).
20. C. Ropp, W. Zhu, A. Yulaev, D. Westly, G. Simelgor, A. Rakholia, W. Lunden, D. Sheredy, M. M. Boyd, S. Papp, A. Agrawal, V. Aksyuk, Integrating planar photonics for multi-beam generation and atomic clock packaging on chip. *Light Sci. Appl.* **12**, 83 (2023).
21. R. Elvin, G. W. Hoth, M. Wright, B. Lewis, J. P. McGilligan, A. S. Arnold, P. F. Griffin, E. Riis, Cold-atom clock based on a diffractive optic. *Opt. Express* **27**, 38359-38366 (2019).

22. B. Lewis, R. Elvin, A. S. Arnold, E. Riis, P. F. Griffin, A grating-chip atomic fountain. *Appl. Phys. Lett.* **121**, 164001 (2022).
23. J. Lee, R. Ding, J. Christensen, R. R. Rosenthal, A. Ison, D. P. Gillund, D. Bossert, K. H. Fuerschbach, W. Kindel, P. S. Finnegan, J. R. Wendt, M. Gehl, A. Kodigala, H. McGuinness, C. A. Walker, S. A. Kemme, A. Lentine, G. Biedermann, P. D. D. Schwindt, A compact cold-atom interferometer with a high data-rate grating magneto-optical trap and a photonic-integrated-circuit-compatible laser system. *Nat. Commun.* **13**, 5131 (2022).
24. S. Eckel, D. S. Barker, J. A. Fedchak, N. N. Klimov, E. Norrgard, J. Scherschligt, C. Makrides, E. Tiesinga, Challenges to miniaturizing cold atom technology for deployable vacuum metrology. *Metrologia* **55**, S182 (2018).
25. C. C. Nshii, M. Vangeleyn, J. P. Cotter, P. F. Griffin, E. A. Hinds, C. N. Ironside, P. See, A. G. Sinclair, E. Riis, A. S. Arnold, A surface-patterned chip as a strong source of ultracold atoms for quantum technologies. *Nat. Nanotechnol.* **8**, 321-324 (2013).
26. J. P. McGilligan, P. F. Griffin, E. Riis, A. S. Arnold, Phase-space properties of magneto-optical traps utilising micro-fabricated gratings. *Opt. Express* **23**, 8948-8959 (2015).
27. J. P. Cotter, J. P. McGilligan, P. F. Griffin, I. M. Rabey, K. Docherty, E. Riis, A. S. Arnold, E. A. Hinds, Design and fabrication of diffractive atom chips for laser cooling and trapping. *Appl. Phys. B* **122**, 172 (2016).
28. C. Huang, H. Liu, L. Chen, C. Li, G. Guo, C. Zao, G. Xiang, Efficient beam flattening for planar-integrated magneto-optical traps. *Chin. Phys. Lett.* **42**, 034203 (2025).
29. Z. Liu, M. Li, S. Wei, Z. Zhan, X. Zhu, X. Liu, Optimized alkali atom cooling scheme using a transmission-grating-based magneto-optical trap. *Opt. Lett.* **50**, 558-561 (2025).
30. O. S. Burrow, P. F. Osborn, E. Boughton, F. Mirando, D. P. Burt, P. F. Griffin, A. S. Arnold, E. Riis, Stand-alone vacuum cell for compact ultracold quantum technologies. *Appl. Phys. Lett.* **119**, 124002 (2021).
31. S. Rotundo, D. Brizi, A. Flori, G. Giovannetti, L. Menichetti, A. Monorchio, Shaping and focusing magnetic field in the human body: State-of-the art and promising technologies. *Sensors* **22**, 5132 (2022).
32. M. C. D. Tayler, K. Mouloudakis, R. Zetter, D. Hunter, V. G. Lucivero, S. Bodenstedt, L. Parkkonen, M. W. Mitchell, Miniature biplanar coils for alkali-metal-vapor magnetometry. *Phys. Rev. Appl.* **18**, 014036 (2022).
33. X. Zhu, C. Liu, H. Su, Y. Miao, H. Cheng, Design of improved four-coil structure with high uniformity and effective coverage rate. *Heliyon* **9**, e15193 (2023).
34. Y. Chen, J. Wang, N. Zhang, J. Wang, Y. Ma, M. Yu, Y. Wang, L. Zhao, Z. Jiang, In situ study of the magnetic field gradient produced by a miniature bi-planar coil for chip-scale atomic devices. *Micromachines* **14**, 1985 (2023).
35. M. Zhang, X. Liu, L. Guo, L. Liu, Y. Cai, Partially coherent flat-topped beam generated by an axicon. *Appl. Sci.* **9**, 1499 (2019).
36. V. Oliner, L. L. Doskolovich, D. A. Bykov, Beam shaping with a plano-freeform lens pair. *Opt. Express* **26**, 19406-19419 (2018).
37. M. Jiang, H. Yu, X. Feng, Y. Guo, I. Chaganava, T. Turiv, O. D. Lavrentovich, Q.-H. Wei, Liquid crystal pancharatnam-berry micro-optical elements for laser beam shaping. *Adv. Opt. Mater.* **6**, 1800961 (2018).
38. H. J. Metcalf, P. Van der Straten, *Laser cooling and trapping* (Springer science & business media, 1999).
39. K. Wang, J. G. Titchener, S. S. Kruk, L. Xu, H. Chung, M. Parry, I. I. Kravchenko, Y. Chen, A. S. Solntsev, Y. S. Kivshar, D. N. Neshev, A. A. Sukhorukov, Quantum metasurface for multiphoton interference and state reconstruction. *Science* **361**, 1104-1108 (2018).
40. W. T. Chen, A. Y. Zhu, F. Capasso, Flat optics with dispersion-engineered metasurfaces. *Nat. Rev. Mater.* **5**, 604-620 (2020).
41. C. Zhang, S. Divitt, Q. Fan, W. Zhu, A. Agrawal, Y. Lu, T. Xu, H. J. Lezec, Low-loss metasurface optics down to the deep ultraviolet region. *Light Sci. Appl.* **9**, 55 (2020).
42. L. Zhu, X. Liu, B. Sain, M. Wang, C. Schlickriede, Y. Tang, J. Deng, K. Li, J. Yang, M. Holynski, S. Zhang, T. Zentgraf, K. Bongs, Y. Lien, G. Li, A dielectric metasurface optical chip for the generation of cold atoms. *Sci. Adv.* **6**, eabb6667 (2020).

43. S. Wang, S. Wen, Z. Deng, X. Li, Y. Yang, Metasurface-based solid poincaré sphere polarizer. *Phys. Rev. Lett.* **130**, 123801 (2023).
44. L. Zeyang, W. Danyan, G. Hao, L. Moxin, Z. Huixian, Z. Cheng, Metasurface-enabled augmented reality display: A review. *Adv. Photonics* **5**, 034001 (2023).
45. M. Jin, X. Zhang, X. Liu, C. Liang, J. Liu, Z. Hu, K. Li, G. Wang, J. Yang, L. Zhu, G. Li, A centimeter-scale dielectric metasurface for the generation of cold atoms. *Nano Lett.* **23**, 4008-4013 (2023).
46. Z. Liu, H. Gao, T. Ma, V. Ray, N. Liu, X. Zhang, L. J. Guo, C. Zhang, Broadband spin and angle co-multiplexed waveguide-based metasurface for six-channel crosstalk-free holographic projection. *eLight* **4**, 7 (2024).
47. Z. Yu, M. Li, Z. Xing, H. Gao, Z. Liu, S. Pu, H. Mao, H. Cai, Q. Ma, W. Ren, J. Zhu, C. Zhang, Genetic algorithm assisted meta-atom design for high-performance metasurface optics. *Opto-Electronic Science* **3**, 240016 (2024).
48. Z. Xing, Z. Lin, N. Liu, H. Gao, Y. Hu, Z. Liu, Z. Jiang, X. Zhang, C. Zhang, Monolithic spin-multiplexing metalens for dual-functional imaging. *Laser Photonics Rev.* **19**, 2401993 (2025).
49. J. Ma, J. Ren, J. Zhang, J. Meng, C. McManus-Barrett, K. B. Crozier, A. A. Sukhorukov, Quantum imaging using spatially entangled photon pairs from a nonlinear metasurface. *eLight* **5**, 2 (2025).
50. S. Moon, S. Kim, J. Kim, C. Lee, J. Rho, Single-layer waveguide displays using achromatic metagratings for full-colour augmented reality. *Nat. Nanotechnol.* **20**, 747-754 (2025).
51. H. Zhou, Z. Xing, Y. Hu, H. Gao, Z. Lin, N. Liu, D. Zheng, X. Zhang, C. Zhang, Compact generation of ultraviolet structured light via low-loss dielectric metasurfaces. *Adv. Opt. Mater.* **n/a**, e01940 (2025).
52. D. Y. Alsaka, Ç. Arpali, S. A. Arpali, M. F. Altemimi, Dynamic flat-topped laser beam shaping method using mixed region amplitude freedom algorithm. *Appl. Phys. B* **128**, 137 (2022).
53. W. R. McGehee, W. Zhu, D. S. Barker, D. Westly, A. Yulaev, N. Klimov, A. Agrawal, S. Eckel, V. Aksyuk, J. J. McClelland, Magneto-optical trapping using planar optics. *New J. Phys.* **23**, 013021 (2021).
54. H. A. N. Yanxu, W. Bo, M. A. Jie, X. Jintao, W. Hai, Measurement of the number and temperature of the cold atoms in medium. *Acta Sin. Quantum Opt.* **13**, 30-34 (2007).
55. J. Duan, X. Liu, Y. Zhou, X. Xu, L. Chen, C. Zou, Z. Zhu, Z. Yu, N. Ru, J. Qu, High diffraction efficiency grating atom chip for magneto-optical trap. *Opt. Commun.* **513**, 128087 (2022).
56. X. Liu, J.-M. Mérolla, S. Guérandel, C. Gorecki, E. de Clercq, R. Boudot, Coherent-population-trapping resonances in buffer-gas-filled Cs-vapor cells with push-pull optical pumping. *Phys. Rev. A* **87**, 013416 (2013).
57. X. Liu, V. I. Yudin, A. V. Taichenachev, J. Kitching, E. A. Donley, High contrast dark resonances in a cold-atom clock probed with counterpropagating circularly polarized beams. *Appl. Phys. Lett.* **111**, 224102 (2017).
58. Z. L. Newman, V. Maurice, C. Fredrick, T. Fortier, H. Leopardi, L. Hollberg, S. A. Diddams, J. Kitching, M. T. Hummon, High-performance, compact optical standard. *Opt. Lett.* **46**, 4702-4705 (2021).
59. M. Abdel Hafiz, D. Brazhnikov, G. Coget, A. Taichenachev, V. Yudin, E. de Clercq, R. Boudot, High-contrast sub-doppler absorption spikes in a hot atomic vapor cell exposed to a dual-frequency laser field. *New J. Phys.* **19**, 073028 (2017).
60. C. Zhang, N. Hong, C. Ji, W. Zhu, X. Chen, A. Agrawal, Z. Zhang, T. E. Tiwald, S. Schoeche, J. N. Hilfiker, L. J. Guo, H. J. Lezec, Robust extraction of hyperbolic metamaterial permittivity using total internal reflection ellipsometry. *ACS Photonics* **5**, 2234-2242 (2018).